Journal of Magnetic Resonance **140,** 305–314 (1999)
Article ID jmre.1998.1655, available online at http://www.idealibrary.com on IDEAL®

Density Matrix Simulations of the Effects of *J* Coupling in Spin Echo and Fast Spin Echo Imaging

L. A. Stables,* R. P. Kennan,† A. W. Anderson,*,† and J. C. Gore*,[1]

**Department of Applied Physics and †Department of Diagnostic Radiology, Yale University School of Medicine, New Haven, Connecticut 06520-8042*

Received March 18, 1998; revised November 3, 1998

A computer simulation has been used to calculate the effects of *J* coupling on the amplitudes of echoes produced by CPMG sequences. The program computes the evolution of the density matrix for different pulse intervals and can predict the signals obtainable from spin systems of any size and complexity. Results from the simulation confirm the prediction that a decrease in the effects of *J* coupling is largely responsible for the bright fat signal seen in fast spin echo imaging at high pulse rates. The effects of *J* coupling on CPMG echotrains are examined for A_3B_2 and $A_3B_2C_2$ spin systems over a wide range of *J* coupling and chemical shift values and pulse spacings. The effects of *J* coupling on the point spread function obtained with fast spin echo imaging are also discussed.

Key Words: J **coupling; density matrix; numerical simulation; FSE; spin echo; pulse sequence.**

INTRODUCTION

Spin-echo (SE) imaging possesses considerable flexibility for manipulating T_1 and T_2 tissue contrast and is often considered to be the reference standard by which other MR imaging techniques are judged. Since the introduction of fast spin-echo (FSE) imaging, in which several echoes that are phase encoded to different degrees are acquired following each excitation, numerous papers have been published directly comparing the characteristics of FSE images to those of conventional SE images (*1–3*). These studies have shown that FSE images provide similar degrees of control over T_1 and T_2 contrast as SE images, as well as comparable tissue differentiation and image detail (*2*). However, when FSE images are acquired with particularly rapid pulse rates, the signals from tissues such as fat and the substantia nigra are much brighter than in SE images. Several previous reports have proposed that the bright fat signal that occurs when short echo spacings are used is caused by a suppression of *J* coupling effects (*2–5*).

The dependence of the NMR signal on the spacing of refocusing pulses in multiecho sequences has been demonstrated experimentally in a number of complex *J*-coupled systems, among them: corn/vegetable/olive oil (*4, 6–10*), diethyl ether (*4, 11*), pork fat (*4*), and bone marrow (*12*). These studies all find an increase in the signal from *J*-coupled nuclei as the pulse spacings decrease. The theoretical explanation of this phenomenon was provided by Allerhand, who derived an expression for the CPMG signal from *J* coupled systems (*13*). He showed that if the spacing of the refocussing pulses was short enough, the effects of *J* coupling disappear. However, the pulse rates in most SE and FSE imaging sequences of practical interest fall short of the strict fast pulse requirement; thus the solution in this limit merely provides a qualitative understanding of signal behavior. In addition, Allerhand's equation for the signal produced in CPMG sequences outside of the ultra-fast pulse regime has closed form solutions only for simple spin systems. As a result, the effects of *J* coupling for complex spin systems, or situations comparable to those experienced with imaging *in vivo*, have not previously been analyzed quantitatively.

This paper presents the results of numerical simulations of the effects of *J* coupling on SE and FSE signals, as well as experiments to verify the accuracy of the simulations. The solution of Allerhand's equation requires the construction and manipulation of large matrices and is therefore well suited to the numerical analysis described here. Several papers have previously been published describing the use of computer programs to analyze the effects of complex pulse sequences (*14–17*). The simulations described here are unique because of their flexibility in handling spin systems of arbitrary complexity and CPMG sequences of any length. We used the simulations to study the behavior of the signal produced in multiecho sequences from a number of relevant spin systems in tissues. These calculations clarify how the effect of *J* coupling varies with chemical shift and *J* coupling parameters and with pulse spacing.

In addition to showing a brighter signal from fat, FSE images also may exhibit increased blurring and ghosting artifacts in the phase-encode direction because the amplitudes of each echo in an echo train are different. While these artifacts can be explained in part by the T_2 decay which occurs between acquisitions of lines in *k*-space, they are also affected by the modulation of the echo train by *J* coupling. Therefore, we also investigated the influence of *J* coupling effects on the point spread function of FSE images.

[1] To whom correspondence should be addressed. E-mail: john.gore@yale.edu.

1090-7807/99 $30.00

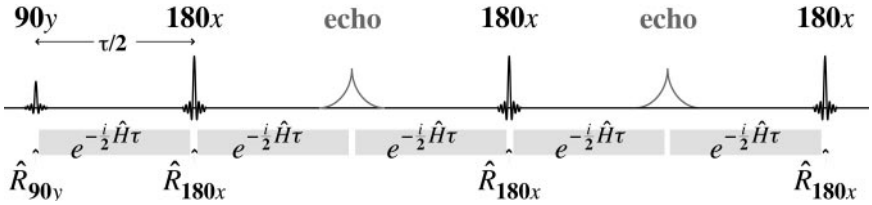

FIG. 1. Operators acting on the density matrix during a pulse sequence. $\hat{R}_{90y}$ and $\hat{R}_{180x}$ are the 90°_y and 180°_x pulse operators, $\hat{H}$ is the Hamiltonian of the system and $\exp(-i\hat{H}t)$ is the time evolution operator.

THEORY

Evolution of the Density Matrix in an FSE Sequence

J coupling is a quantum mechanical phenomenon with no classical analog, and therefore its effect on nuclear magnetization must be studied using an appropriate quantum mechanical formalism. Given that we are interested in the *ensemble* behavior of the nuclear spins, we use the density matrix to follow the development of the system during the CPMG pulse sequence.

The signal measured in a magnetic resonance experiment is proportional to (*18*)

$$\langle \hat{I}_x(t) \rangle = \mathrm{Tr}[\hat{\rho}(t)\hat{I}_x], \qquad [1]$$

where $\hat{I}_x$ is the x component of the total angular momentum operator. For a time independent Hamiltonian, the time dependence of ρ, the density matrix of the system, is given by

$$\hat{\rho}(t) = \exp(-i\hat{H}t)\hat{\rho}_0\exp(i\hat{H}t), \qquad [2]$$

where $\hat{\rho}_0$ is the density matrix at $t = 0$, $\hat{H}$ is the Hamiltonian of the system and $\exp(-i\hat{H}t)$ is the time evolution operator. Therefore, the effect of *J* coupling on the signal measured using a CPMG sequence can be determined by following the time evolution of $\rho(t)$ through each phase of the sequence. Figure 1 shows a diagram of the operators acting on the density matrix in the course of a CPMG experiment. The expression for the density matrix at the n'th echo is (*13*)

$$\hat{\rho}(n\tau) \propto (e^{-i/2\hat{H}\tau}\hat{R}_{180x}e^{-i/2\hat{H}\tau})^n\hat{I}_x(e^{-i/2\hat{H}\tau}\hat{R}_{180x}e^{-i/2\hat{H}\tau})^{-n}, \qquad [3]$$

where τ is the spacing between 180°_x pulses. The operators are

$$\hat{I}_x = \sum_i \hat{I}_{xi} \qquad [4]$$

and the rotation operator for the 180°_x pulse,

$$\hat{R}_{180x} = \exp(i\pi\hat{I}_x). \qquad [5]$$

The Hamiltonian is given by

$$\hat{H} = -\sum_j \delta_j\hat{I}_{zj} - \sum_{j<k} J_{jk}\hat{I}_j \cdot \hat{I}_k, \qquad [6]$$

where J_{jk} is the *J* coupling constant between spins j and k, and δ_j is the chemical shift of nucleus j with respect to the average Larmor frequency of the spins. A term containing the overall chemical shift of the system and terms which do not involve chemical shift or *J* coupling are omitted from the Hamiltonian as they do not affect the following calculations.

Combining Eqs. [1] and [3] gives the final expression for the signal:

$$\begin{aligned} S(n\tau) &\propto \langle \hat{I}_x(n\tau) \rangle \\ &\propto \mathrm{Tr}[(e^{-i/2\hat{H}\tau}\hat{R}_{180x}e^{-i/2\hat{H}\tau})^n\hat{I}_x \\ &\times (e^{-i/2\hat{H}\tau}\hat{R}_{180x}e^{-i/2\hat{H}\tau})^{-n}\hat{I}_x]. \end{aligned} \qquad [7]$$

The effect of T_2 relaxation has been omitted for clarity, but can be included by multiplying the RHS of Eq. [7] by $\exp(-n\tau/T_2)$. Note that in Eq. [7], the time evolution operator, $\exp(-i/2\hat{H}\tau)$, is a function solely of terms containing $J_{jk}\tau$ and $\delta_j\tau$. As a result the signal at any echo in a CPMG train depends on the products, $J_{jk}\tau$ and $\delta_j\tau$, not on J_{jk}, δ_j, or τ individually. Finally, the contribution of a specific spin, j, to the signal can be obtained by substituting $\hat{I}_{xj}$ for the final $\hat{I}_x$ in Eq. [7].

Equation [7] is not simplifiable because $\hat{H}$ and $\hat{R}_{180x}$ do not commute. As a result, analytic solutions to this expression are exceedingly difficult to find. However, in the matrix representation that diagonalizes $\exp(-i/2\hat{H}\tau)\hat{R}_{180x}\exp(-i/2\hat{H}\tau)$, Eq. [7] becomes

$$S(n) \propto \sum_j |\langle \xi_j|\hat{I}_x|\xi_j\rangle|^2 + 2\sum_{j<k} |\langle \xi_j|\hat{I}_x|\xi_k\rangle|^2\cos[n(\lambda_j - \lambda_k)], \qquad [8]$$

where the ξ_j are the eigenfunctions of $\exp(-i/2\hat{H}\tau)\hat{R}_{180x}\exp(-i/2\hat{H}\tau)$, and $\exp(i\lambda_j)$ are the corresponding eigenvalues (*13*). Equation [8] can be written in the form

$$S(n) \propto c_o + \sum_{m=1}^{M} c_m \cos(\omega_m n), \quad [9]$$

where the coefficients c_m and ω_m are real and $M \leq 2^N(2^N - 1)$ (N = number of spins in the system). Thus, in the absence of relaxation, this equation shows that for a multiple spin system, the amplitudes of the echoes in a CPMG train are modified by a large but finite number of frequencies. The values of c_m and ω_m depend solely on the relative chemical shifts (δ_j) and coupling constants (J_{jk}) of the system and on τ. In the simplest case of a weakly coupled two spin system, Eq. [8] reduces to the familiar result,

$$S(n) \propto \cos(\pi J n \tau). \quad [10]$$

S(n) in the Fast Pulse Rate Limit

In the limit that

$$|J_{jk}|\tau \text{ and } |\delta_{jk}|\tau \ll 1, \ \forall\, j, k, \quad [11]$$

the term $\exp(-i/2\hat{H}\tau)$ can be expanded to first order in Eq. [3]. As shown in Ref. (*13*), the chemical shift terms disappear in this limit and the remaining operators commute. As a result, the density matrix remains constant over time and

$$S(n) = S(0) \propto \mathrm{Tr}[\hat{I}_x^2]. \quad [12]$$

Thus, when τ becomes sufficiently small, the echo train modulation caused by J coupling disappears. Without this modulation, the signal from J coupled spins at any echo time becomes substantially greater. This is the cause of the brighter fat signal seen in FSE images.

COMPUTER SIMULATIONS OF ALLERHAND'S EQUATION

Analytic solutions for Eq. [7]/[8] have been published only for the AB, A_2B, and A_3B spin systems (*13*). The pulse rates in most SE and FSE imaging sequences of practical interest fall short of the fast pulse regime in which Eq. [7] reduces to Eq. [12]; thus the fast pulse solution gives only limited insight into the expected signal behavior.

To understand the role of J coupling in pulse rate regimes of clinical interest, it is necessary to solve Eq. [7] or [8] for complex spin systems outside of the fast pulse limit. Because the quantum mechanical operators discussed above can be represented as matrices, the solution of Eqs. [7]–[8] can be converted into a matrix algebra problem that can be solved numerically. With this in mind, we developed a series of computer programs that solve these equations. We then used the programs to obtain the SE/FSE signal behavior of a number of spin systems similar to those of biological interest.

The simulations construct matrix representations of the necessary operators and then use them to solve either Eq. [7] or [8]. The details of the algorithm are discussed in the Appendix. The programs were written in MATLAB (Mathworks, Natick, MA), a language that is particularly well suited for simulations that require substantial matrix manipulations.

In addition to calculating the signal from the entire spin system, the programs calculate the contributions of individual nuclei to the overall signal. They are capable of solving Eqs. [7]–[8] for spin systems of arbitrary size and complexity, provided the computer has enough memory to handle the resulting $2^N \times 2^N$ matrices. The only parameters needed to characterize a given spin system are the chemical shifts of its protons and their respective J couplings. The pulse sequence is characterized by the pulse spacing, τ, and the length of the pulse sequence (on which there are no restrictions).

If needed, the programs can also calculate the magnetization at any time between echo peaks by solving the equations

$$\hat{\rho}(n\tau + t) \propto \begin{cases} e^{-i\hat{H}t}\hat{\rho}(n\tau)e^{i\hat{H}t} & t < \dfrac{\tau}{2} \\ e^{-i\hat{H}t}\hat{R}_{180x}e^{-i/2\hat{H}\tau}\hat{\rho}(n\tau)e^{i/2\hat{H}\tau}\hat{R}_{180x}e^{i\hat{H}t} & t > \dfrac{\tau}{2} \end{cases}. \quad [13]$$

To verify the accuracy of the simulation results, the simulated echo trains for a range of A_2B spin systems were compared to the echo trains obtained from Allerhand's analytical solutions for these systems. The simulation results agreed with Allerhand's to within 1 part per billion. In addition, we used the program's ability to generate a theoretical FID (from Eq. [13]), to predict the spectra of a number of A_3B_2 systems. The theoretical FID's for these systems were calculated and then Fourier-transformed to obtain their NMR spectra. The locations and magnitudes of peaks in these spectra were identical to the theoretical spectral peaks tabulated by Emsley (*19*) for A_3B_2 systems with identical values of J/δ.

In order to clarify the manner in which the effects of J coupling depend on spin system and pulse sequence parameters, we studied a number of hypothetical strongly coupled A_3B_2 and $A_3B_2C_2$ spin systems over a wide range of values of δ_{AB} ($=|\delta_A - \delta_B|$), J_{AB}, and τ. In addition, we simulated the SE and FSE behaviors of a specific molecule, 1-pentene ($CH_3CH_2CH_2CH = CH_2$), which was chosen as a model for the hydrocarbon chains found in lipids. The sizes of true lipids, which typically contain 30 or more protons, makes simulation of their NMR behavior prohibitive—1-pentene was chosen because, as a ten-spin system, it was the largest hydrocarbon chain that our simulation could conveniently handle. The J coupling values and chemical shifts for the protons in 1-pentene were first estimated from values given in the literature for 1-hexene, 1-propene, and 1-butene (*20, 21*). These estimates were then fine-tuned by matching the theoretical spectra they

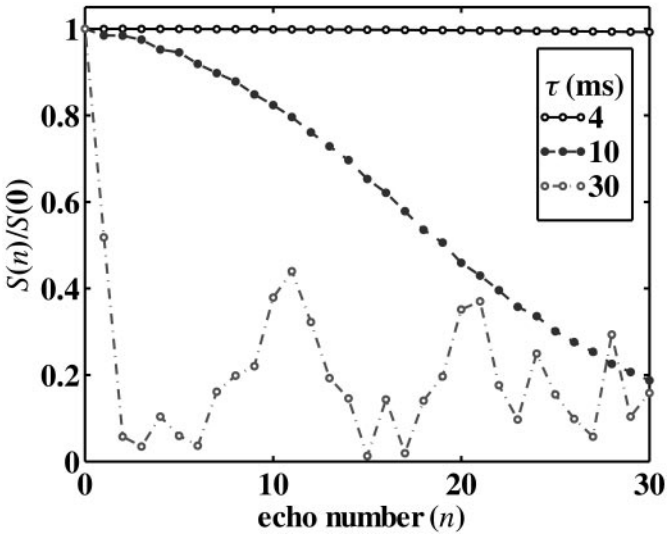

FIG. 2. The effect of J coupling on a strongly coupled A_3B_2 spin system. The plot shows signal vs echo number for CPMG sequences where τ, the spacing between echoes, is 4, 10, or 30 ms. $\delta_{AB} = 40$ Hz, $J_{AB} = 6$ Hz. Intrinsic T_2 relaxation is neglected. These three curves illustrate the general tendency of J coupling modulation to fall into one of 2 regimes: smooth or erratic modulation.

produced to a high-resolution (7T) spectrum of 1-pentene (*22*). Labeling the 1-pentene protons as $A_3B_2C_2DEF$ (where E is *cis* to D, F is *trans*), the chemical shift values obtained were: $\delta_A = .91$ ppm, $\delta_B = 1.41$ ppm, $\delta_C = 2.02$ ppm, $\delta_D = 5.80$ ppm, $\delta_E = 4.93$ ppm, and $\delta_F = 5.00$ ppm. The J coupling values were $J_{AB} = 7.5$ Hz, $J_{BC} = 6.5$ Hz, $J_{CD} = 6.3$ Hz, $J_{CE} = -1.2$ Hz, $J_{CF} = -1.6$ Hz, $J_{DE} = 10$ Hz, $J_{DF} = 17$ Hz, and $J_{EF} = 2.5$ Hz.

In addition to the computer simulations, the SE and FSE signals from 1-pentene were measured experimentally. Measurements of 1-pentene samples contained in 8-mm test tubes were performed at 2.0 T on a GE Omega imaging spectrometer.

SIMULATION AND EXPERIMENTAL RESULTS

For the simulation data shown below, the absolute value of the signal is shown relative to its value in the absence of J coupling. The figures show the effects of J coupling only; the additional decay due to intrinsic T_2 relaxation is omitted for clarity.

A_3B_2 Systems

Figure 2 shows the effect of J coupling on the echotrains of a strongly coupled A_3B_2 spin system with $\delta_{AB} = 40$ Hz and $J_{AB} = 6$ Hz. These J coupling and chemical shift values are representative of those found in hydrocarbon chains at 2 T: the system thus models the CH_3CH_2 spin groups typically found at the end of hydrocarbon chains. Echotrains are shown at three values of τ to illustrate the effect that this parameter has on the CPMG signal. When $\tau = 4$ ms, the echotrain is barely modulated. As τ increases, the degree of modulation of the echotrain steadily increases, but remains smoothly varying, as seen in the $\tau = 10$ ms echotrain. However, at $\tau = 30$ ms ($\delta_{AB}\tau = 1.2$), the signal drops off abruptly at the first and second echoes and then varies unpredictably.

The dependence shown in Fig. 2 of the echotrain on τ is representative of the behavior seen in all of our simulations. Above a threshold of τ which depends on the values of J and δ in the system, the behavior of the echotrain is erratic and difficult to characterize. Below this threshold, the echotrain varies smoothly, its modulation decreasing as τ decreases. The transition between the regimes of smooth and erratic modulation is very abrupt: in the A_3B_2 spin system discussed above, the transition occurs between $\tau = 20$ and 21 ms.

The transition from smooth to erratic J coupling modulation can be best understood by analyzing the cosinusoidal terms that make up each echotrain (Eq. [9]). Because n in Eq. [9] is restricted to integer values, the mth component of the signal, $\cos(\omega_m n)$, is sampled at a rate of $2\pi/\omega_m$ points per period. As ω_m increases, $\cos(\omega_m n)$ becomes less smoothly sampled: above a threshold of roughly $\omega_m = \pi/3$, a plot of $\cos(\omega_m n)$ ceases to look cosinusoidal. As a result, any component of the echotrain which oscillates above $\omega_m = \pi/3$ will make an erratic contribution to the signal. Figure 3 shows the normal-

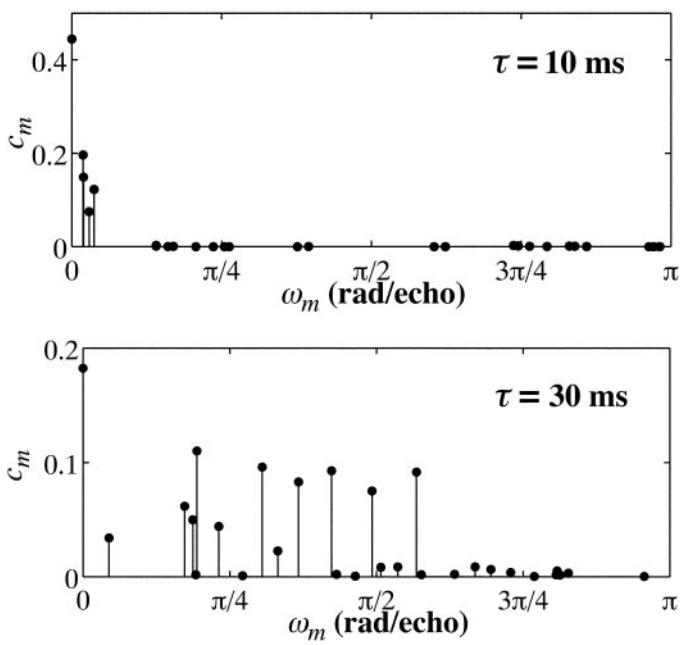

FIG. 3. The normalized amplitudes of the frequency components of the $\tau = 10$- and 30-ms echotrains shown in Fig. 2. The 10-ms echotrain has a large unmodulated component as well as a few low frequency components. The result is a smoothly varying echotrain. The range of frequencies contributing to the CPMG signal increases steadily with increasing τ, and the size of the unmodulated component decreases. The presence of terms where $\omega > \pi/3$ causes the erratic modulation of the 30-ms echotrain.

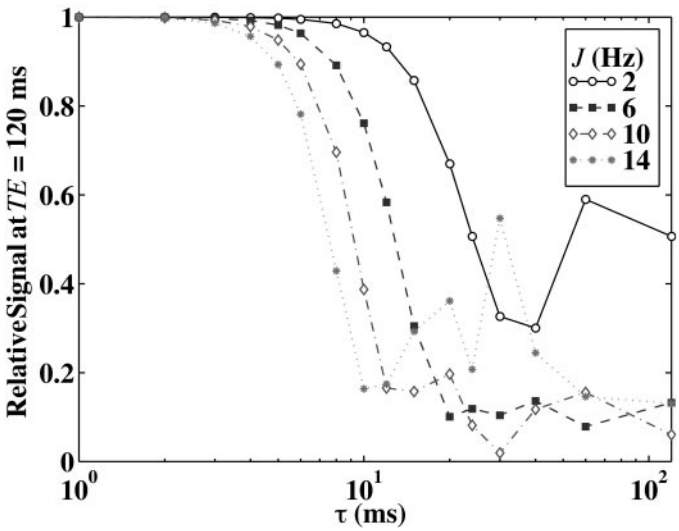

FIG. 4. CPMG signal at $TE = 120$ ms vs τ for a set of A_3B_2 systems with $\delta_{AB} = 40$ Hz and $J_{AB} = 2$ to 14 Hz. τ ranges from 1 to 120 ms. At $\tau = 10$, 12, 20, or 30 ms (for $J = 14$, 10, 6, or 2 Hz, respectively), the dependence of the signal on τ abruptly becomes unpredictable, reflecting a transition into a regime of erratic J modulation.

ized amplitudes, c_m, and frequencies, ω_m, of the components of the $\tau = 10$ and 30 ms echotrains shown in Fig. 2. Clearly, many of the significant terms contributing to the 30 ms echotrain oscillate at frequencies well above $\pi/3$ and thus will not be smoothly sampled. The only substantial contributions to the 10-ms echotrain come from a handful of low frequency components: these terms make a smoothly varying contribution to the modulation. In addition, the zero frequency component is much larger in the 10-ms echotrain. In general, as τ increases, the unmodulated component of the echotrain decreases and the range of frequencies represented in the echotrain becomes steadily broader. A similar broadening (of the range of frequencies contributing to the echotrain) occurs as any values of J or δ in a system increase.

In Fig. 3, the number of frequency components in both echotrains is 29. This is substantially smaller than the $2^5(2^5 - 1)$ possible combinations of $\omega_m = |\lambda_j - \lambda_k|$ because many of the differences have the same value or are zero. Furthermore, because n must be an integer, $\cos(\omega_m n) = \cos[(2\pi - \omega_m)n]$. Therefore, all ω_m falling between $[\pi, 2\pi]$ can be mapped to $2\pi - \omega_m$.

Figure 4 shows the CPMG signal at $TE = 120$ ms, as a function of τ. The relative signals were calculated for a set of A_3B_2 spin systems with $\delta_{AB} = 40$ Hz and $J_{AB} = 2$ to 14 Hz. When τ is short, the signal drops off smoothly as either J or τ increases. However, between $\tau = 10$ and 30 ms (depending on J), the curves change abruptly from being smoothly varying to being unpredictable. The signal loss in the erratically coupled regime is much less dependent on the values of J or τ. This again reflects the unpredictable manner in which J coupling modulates the echo train for larger τ. Note that the value of τ at which the transition to erratic modulation occurs does not vary linearly with $1/J$—this is because the value of $\delta_{AB}\tau$ also determines when this transition occurs.

The simulations suggest that because J coupling can cause the signal in an echo train to fall off dramatically, its effects mimic those of T_2 relaxation, although the decay is clearly nonexponential. In order to estimate an "effective" T_2 for an echo train, we fit the initial monotonic portion of the signal

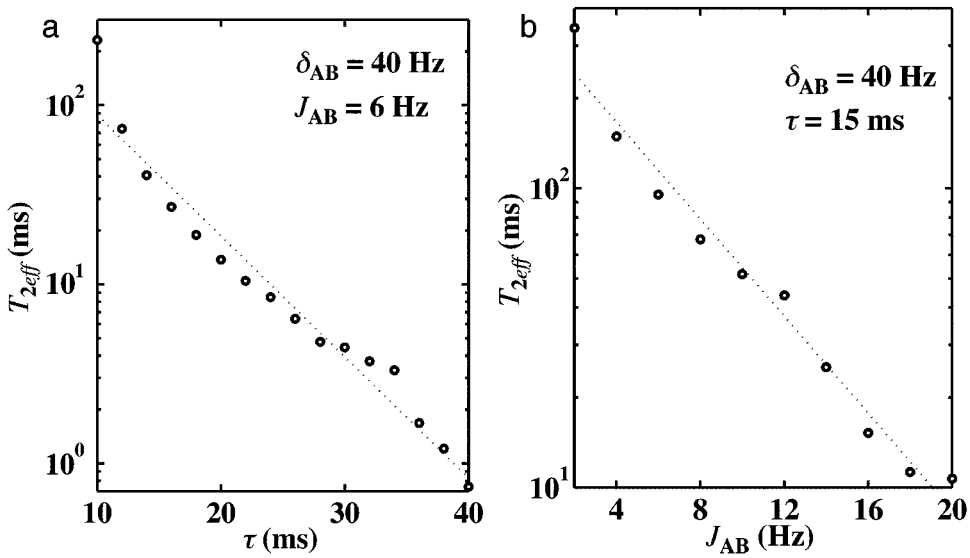

FIG. 5. "Effective" T_2 as a function of τ and J for echo trains of A_3B_2 systems. T_{2eff} was estimated by fitting the initial portion of each echo train to an exponential decay. In (a) $J_{AB} = 6$ Hz and $\tau = 10$ to 40 ms, while in (b) $\tau = 15$ ms and $J = 2$ to 20 Hz. As either τ or J increases, T_{2eff} decreases at an approximately exponential rate.

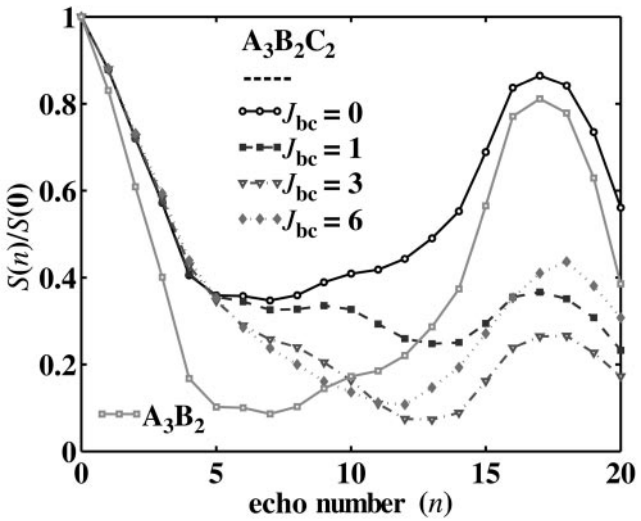

FIG. 6. The effect of additional J coupled spins on a system. For the $A_3B_2C_2$ spin systems, $\delta_{AB} = \delta_{AC} = 40$ Hz, $J_{AB} = 6$ Hz, and $J_{AC} = 0$ Hz. An A_3B_2 echotrain with identical values of δ_{AB} and J_{AB} is also shown for comparison; $\tau = 20$ ms. The $A_3B_2C_2$ echotrains become more modulated as J_{BC} increases, though they are not as strongly modulated as the A_3B_2 echotrain due to the near-equivalence of the B and C spins.

decays to an exponential curve. The results of these fits are shown as a function of τ and J_{AB} in Fig. 5. For an A_3B_2 system with $J_{AB} = 6$ Hz and $\delta_{AB} = 40$ Hz, Fig. 5a shows that T_{2eff} drops at a roughly exponential rate as τ increases. Similar behavior is seen in Fig. 5b, for T_{2eff} vs J. Both figures demonstrate that the effective T_2 can be very short ($<$100 ms). As a result, in strongly coupled systems, the effects of J coupling may dominate the decay of transverse magnetization in CPMG sequences, so that the apparent T_2 of protons in even simple molecules reflects coupling rather than relaxation.

$A_3B_2C_2$ Systems

Figure 6 shows the relative signal of the echo trains of a set of $A_3B_2C_2$ spin systems, where $\delta_{AB} = \delta_{AC} = 40$ Hz, $J_{AB} = 6$ Hz, $J_{AC} = 0$ Hz, and $\tau = 20$ ms. (The B and C spins are not magnetically equivalent because $J_{AB} \neq J_{AC}$.) J_{BC} ranges from 0 to 6 Hz. For reference, the solid gray curve shows the signal decay of an A_3B_2 system with identical values of δ_{AB} and J_{AB}. When $J_{BC} = 0$, the $A_3B_2C_2$ echotrain contains the same frequency components as the A_3B_2 echotrain, but, except for the zero frequency component, the amplitude of each component is smaller since two of the seven spins do not contribute to the modulation. The presence of the uncoupled spins in this system thus dampens the overall effects of J coupling. As J_{BC} increases, the $A_3B_2C_2$ echotrains become more modulated, especially at lower frequencies, though they are still not as strongly modulated as the A_3B_2 echotrain. Because $\delta_{BC} = 0$, the B and C spins approach magnetic equivalence, and so the J coupling between them is less apparent than that between the A and B spins.

1-pentene

Simulated and experimental echotrains for 1-pentene are shown in Fig. 7 for $\tau = 2$, 12, 16, and 20 ms. To match the experimental setup, the simulations were run assuming a field strength of 2 T. At each value of τ, the simulated and experimental echotrains exhibit nearly identical oscillations, though the oscillations of the simulated echotrains are more exaggerated. Both sets of echotrains show the same general features seen in the A_3B_2 data: the echotrain is nearly unmodulated when $\tau = 2$ ms and becomes more modulated as τ increases. A transition between smooth and erratic modulation occurs around $\tau = 20$ ms. The disparity between the amplitudes of the modulation of the simulated and experimental data may arise from effects such as stimulated echoes (from using imperfect refocusing pulses in the experimental measurements), or coherence transfer cross-relaxation phenomena, which are not accounted for in the simulations.

DISCUSSION

The erratic echotrain behavior observed in our studies of A_3B_2 systems and 1-pentene has also been observed experimentally in studies of diethyl ether, a strongly coupled A_3B_2 system (*4, 11*). However, measurements of the pulse spacing dependence of lipids such as corn oil and pork fat have found a smooth pulse spacing dependence (*4, 6, 8, 10*). The differences between the CPMG signal behavior of lipids and systems such as 1-pentene may arise from the longer chains of saturated methylene (CH_2) protons in lipids. The chemical shift differences between these neighboring methylene groups are very small and, as Fig. 6 demonstrates, this can lead to a dampening of the effects of J coupling.

The Point Spread Function of J Coupled Echotrains

T_2 decay occurs during the acquisition of data in a CPMG experiment, so successive echoes (and hence different lines in **k**-space in FSE) have smaller amplitudes. This effect alone can cause blurring in the phase encode direction of an image (*1, 23, 24*). The presence of J coupling induced modulation in the echotrain will further affect the image point spread function (PSF), as has been demonstrated for weakly coupled spin systems [Chao, 1997 #96; Duyn, 1995 #95]. In this section we derive expressions for the PSF due to the effects of J coupling.

Assuming that the phase encode direction is y, the signal in an FSE image can be written as the convolution (*24*)

$$f_{\mathrm{FSE}}(x, y) = h_{JC}(y) * h_{T2}(y) * f_{\mathrm{SE}}(x, y), \qquad [14]$$

where h_{JC} is the point spread function (PSF) due to J coupling, h_{T2} is the PSF due to T_2 decay, and f_{SE} is the signal in a SE image of the same region. h_{JC} is given by

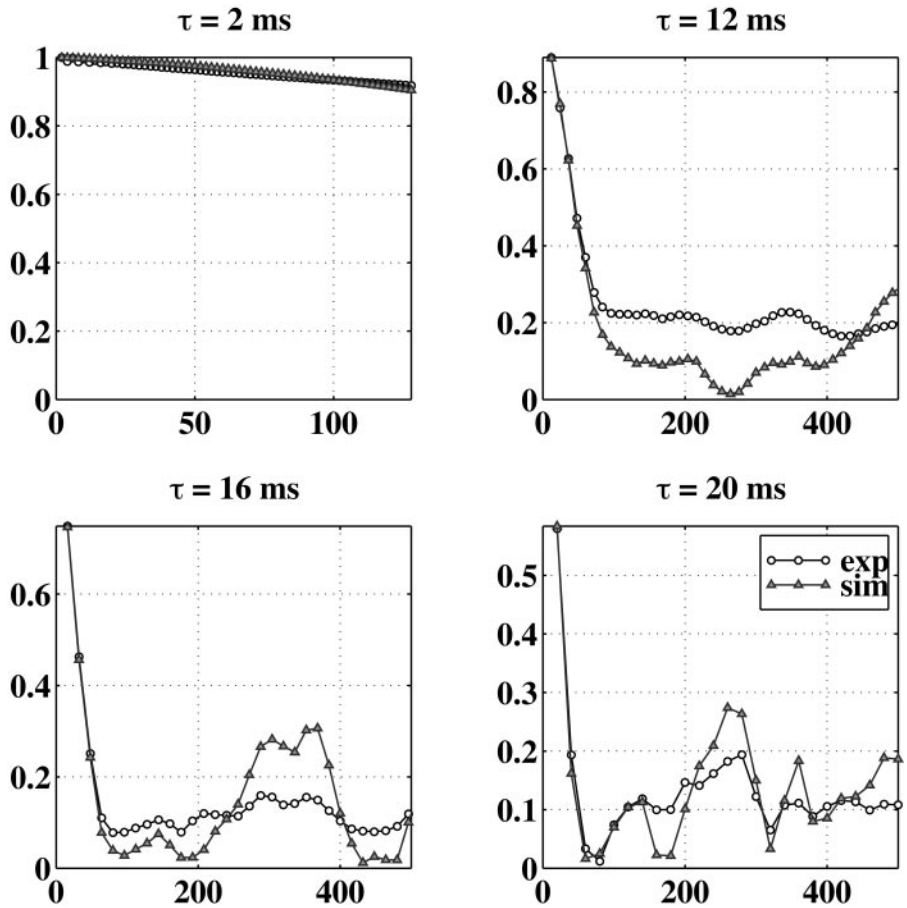

FIG. 7. Simulated and experimental echotrains for 1-pentene for $\tau = 2$, 12, 16, and 20 ms; $B_0 = 2$ T. The echotrains again show a transition from smooth to erratic modulation as τ increases. Conversely, as τ decreases, the effects of J coupling disappear.

$$h_{JC}(y) = \int_{-\infty}^{\infty} S[n(k_y)]e^{-ik_y y}dk_y$$

$$= \sum_{m=0}^{M} c_m \int_{-\infty}^{\infty} \cos[\omega_m n(k_y)]e^{-ik_y y}dk_y, \qquad [15]$$

where c_m and ω_m are the coefficients used in Eq. [9] (where $\omega_0 = 0$), n is the echo number, and k_y denotes the position along the phase encode axis of **k**-space. The PSF will clearly depend on $n(k_y)$, which defines the order in which phase encode steps are acquired. One possible ordering scheme, where positive and negative values of k_y have the same dependence on n, is shown in Fig. 8a. $n(k_y)$ is given by

$$n = 1 + |k_y|/\Delta k_y \quad -k_{y\max} \le k_y \le k_{y\max}. \qquad [16]$$

Equation [16] describes an imaging scheme which uses two spin excitations to fill **k**-space, but can also approximate schemes which use a greater number of excitations. Inserting Eq. [16] into [15] yields

$$h_{JC}(y) = \sum_{m=0}^{M} c_m \left[\pi \cos(\omega_m)\delta(|y| - y_m) + 2 \sin(\omega_m) \frac{y_m}{y^2 - y_m^2} \right], \qquad [17]$$

where

$$y_m = \omega_m/\Delta k_y = \omega_m l/\pi,$$

and $2l$ is the field of view of the image in the y direction.

A monotonic trajectory (such as for a single excitation sequence) may also be used, where

$$n = n_0 + k_y/\Delta k_y, \qquad [18]$$

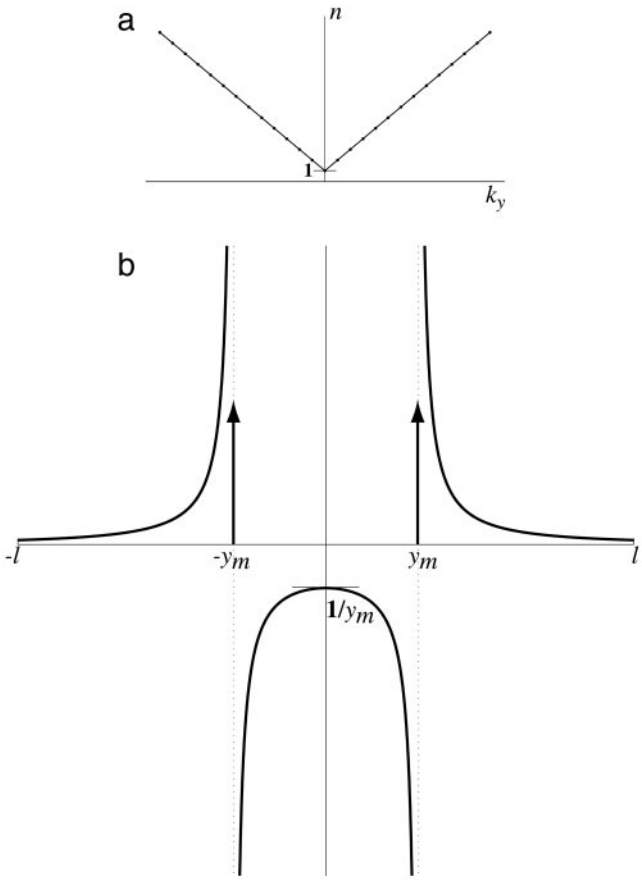

FIG. 8. (a) The phase encode ordering for the FSE acquisition scheme described by Eq. [16]. (b) The contribution of a modulation at frequency ω_m (where $\omega_m = \pi/3$) to the PSF of an FSE image, assuming the $n(k_y)$ shown in (a). The arrows at $\pm y_m$ denote Dirac δ functions of magnitude $\pi c_m \cos(\omega_m)$.

and n_0 is the echo at which the zeroth order phase encode step is acquired. In that case,

$$h_{JC}(y) = \sum_{m=0}^{M} c_m\{\pi \cos(\omega_m n_0)\delta(|y| - y_m) + i\pi \sin(\omega_m n_0) \times [\delta(y - y_m) - \delta(y + y_m)]\}. \quad [19]$$

The imaginary terms result from the fact that $n(k_y)$ is not even.

A plot of Eq. [17] for a single value of ω_m is shown in Fig. 8b. Note that because $0 \leq \omega_m \leq \pi$, the limits of y_m are $[0, l]$. The δ functions at $\pm y_m$ in the PSF will introduce image ghosts, with the J coupled portions of the image shifted by $\pm y_m$. The terms of the form $y_m/(y^2 - y_m^2)$ resemble approximations of $\pm\delta'(y - y_m)$ (where $'$ denotes the derivative). Since

$$f(y)*\delta'(y - y_m) = f'(y - y_m), \quad [20]$$

the effects of convolution with these terms resemble ghosts of the derivative of the J coupled regions.

CONCLUSION

The computer simulations described in this paper have provided a powerful tool to examine the effects of J coupling in a variety of spin systems. They demonstrate that in general, for pulse rates typical of conventional spin echo sequences, the presence of J coupling in a system dephases the transverse magnetization substantially. As the values of $J\tau$ and $\delta\tau$ increase, the effect of J coupling progresses from a slight signal attenuation to severe and erratic signal dephasing. The rapid dephasing and erratic modulation are caused by the interference of the large number of discrete frequencies which modulate the echotrain. In the erratic dephasing regime, the signal loss at a specific echo in the train can be as high as 99% relative to the decoupled signal, and this loss may already be apparent in the second or third echo.

Conversely, when the CPMG echo spacing is very short, the J coupling modulation disappears and lipid signals become bright. A modification of the FSE sequence has recently been suggested which suppresses this lipid signal by exploiting the dependence of J coupling effects on pulse spacing (*25, 26*). In the DIET sequence, the first refocusing interval is made longer than subsequent refocusing intervals. This allows a greater mixing of coupled spins during the first echo, which leads to dephasing and hence signal attenuation.

APPENDIX

Simulation Algorithm

To solve Eqs. [7]–[8] using matrix operators, it is first necessary to construct an appropriate set of basis states to represent the system. The most numerically convenient set of basis functions were the eigenstates of the Zeeman Hamiltonian,

$$\hat{H}_z = \omega_o \hat{I}_z = \omega_o \sum_{j=1}^{N} \hat{I}_{zj}, \quad [21]$$

where N is the number of spins in the system and $\hat{I}_{zj}$ is the z component of the angular momentum operator for nucleus j. The basis set is an orthonormal set of simple product wavefunctions representing all possible combinations of the eigenstates, denoted $|+\rangle$ and $|-\rangle$, of $\hat{I}_{zj}$ for each individual nucleus, j. In an N-spin system there are 2^N possible combinations of the $|+\rangle$ and $|-\rangle$ states.

Each product state is represented by an N-term vector, where the jth element in the vector describes the state of spin j. A "1" signifies the spin is in the $|+\rangle$ state, while a "-1" signifies the spin is in the $|-\rangle$ state. The entire set of product wavefunctions is stored in a $2^N \times N$ matrix, P, where each row represents a separate product wavefunction. For a 2-spin system, the matrix of product wavefunctions, P, looks like

$$P = \begin{bmatrix} 1 & 1 \\ 1 & -1 \\ -1 & 1 \\ -1 & -1 \end{bmatrix} \leftrightarrow \begin{matrix} |++\rangle \\ |+-\rangle \\ |-+\rangle \\ |--\rangle \end{matrix} . \quad [22]$$

If the product wavefunctions are denoted $|a_m\rangle$, where $m = 1, \ldots, 2^N$, then

$$\hat{I}_{zj}|a_m\rangle = \tfrac{1}{2} P_{mj}|a_m\rangle, \quad [23]$$

where the eigenvalues are given in units of $\hbar$.

The basis functions are not used explicitly in solving Eq. [7], but are needed to form matrix representations of the $\hat{I}_x$, $\hat{R}_{180x}$, and $\hat{H}$ operators. The matrix representation of each operator can be constructed using

$$X_{mn} \doteq \langle a_m|\hat{X}|a_n\rangle, \quad [24]$$

where $\hat{X}$ is a quantum mechanical operator and the symbol $\doteq$ denotes "is represented by."

The operator $\hat{I}_x$ is equal to $\sum \hat{I}_{xj}$, where the effect of $\hat{I}_{xj}$ on a given wavefunction is to reverse the jth spin state. Consequently, $\hat{I}_x$ generates a series of N product wavefunctions, each differing from the original in only one spin state. In a 2-spin system, for example,

$$\hat{I}_x|++\rangle = \{|-+\rangle + |+-\rangle\}/2. \quad [25]$$

The product functions, $\{|a_m\rangle\}$, are orthonormal; therefore when Eq. [24] is applied to construct the matrix representation of $\hat{I}_x$ in the Zeeman basis, $I_{xmn} = \frac{1}{2}$ only if $|a_m\rangle$ and $|a_n\rangle$ differ in one (and only one) of their spinstates. For a 2 spin system,

$$\mathbf{I_x} \doteq \frac{1}{2} \begin{array}{c} \begin{matrix} |++\rangle & |+-\rangle & |-+\rangle & |--\rangle \end{matrix} \\ \begin{bmatrix} 0 & 1 & 1 & 0 \\ 1 & 0 & 0 & 1 \\ 1 & 0 & 0 & 1 \\ 0 & 1 & 1 & 0 \end{bmatrix} \end{array} \begin{matrix} |++\rangle \\ |+-\rangle \\ |-+\rangle \\ |--\rangle \end{matrix} . \quad [26]$$

The product states are shown along the sides of [26] to clarify their ordering. It is also possible to calculate matrix representations of $\hat{I}_{xj}$, which are needed if one would like to calculate the contribution of the jth nuclei to the signal. The nonzero elements of $\mathbf{I_{xj}}$ are those connecting wavefunctions that differ solely in the jth spin state.

The 180° rotation operator, $\hat{R}_{180x}$, can be written in the form

$$\hat{R}_{180x} = (2i)^N \prod_{j=1}^{N} \hat{I}_{xj}. \quad [27]$$

The operator therefore flips every spin state in a product wavefunction. In a 4-spin system,

$$\hat{R}_{180x}|+-++\rangle = |-+--\rangle. \quad [28]$$

To construct the matrix representation of $\hat{R}_{180x}$, the simulation compares each pair of wavefunctions and assigns a value of i^N only when the spin states of $|a_m\rangle$ and $|a_n\rangle$ are exactly opposite one another. For a 2-spin system,

$$\mathbf{R} \doteq \begin{bmatrix} 0 & 0 & 0 & -1 \\ 0 & 0 & -1 & 0 \\ 0 & -1 & 0 & 0 \\ -1 & 0 & 0 & 0 \end{bmatrix} \quad [29]$$

The final matrix needed to solve Eqs. [7]–[8] is the Hamiltonian,

$$\hat{H} = -\sum_j \delta_j \hat{I}_{zj} - \sum_{j<k} J_{jk} \hat{\mathbf{I}}_j \cdot \hat{\mathbf{I}}_k. \quad [30]$$

The values of δ_j and J_{jk} are contained in $1 \times N$ and an $N \times N$ matrices, which can be read from an input file. The dot product $\hat{\mathbf{I}}_j \cdot \hat{\mathbf{I}}_k$ in the Hamiltonian can be expanded to give (*27*)

$$\hat{\mathbf{I}}_j \cdot \hat{\mathbf{I}}_k = \hat{I}_{jz}\hat{I}_{kz} + \tfrac{1}{2}(\hat{I}_{j+}\hat{I}_{k-} + \hat{I}_{j-}\hat{I}_{k+}). \quad [31]$$

$\hat{I}_+$ and $\hat{I}_-$ are the raising and lowering operators, where

$$\begin{aligned} \hat{I}_+|+\rangle &= 0 \qquad \hat{I}_-|+\rangle = |-\rangle \\ \hat{I}_+|-\rangle &= |+\rangle \quad \hat{I}_-|-\rangle = 0. \end{aligned} \quad [32]$$

The $\hat{I}_{j+}\hat{I}_{k-}$ operator only returns a nonzero product state when the j nucleus is in the $|-\rangle$ state and the k nucleus is in the $|+\rangle$ state. The reverse is true for the $\hat{I}_{j-}\hat{I}_{k+}$ operator. Viewed together, the final 2 terms of [31] only affect product states having a pair of spins in opposite states. The simulation therefore looks for pairs of wavefunctions which differ in the spinstates of two (and only two) of the nuclei, and then checks if these two nuclei have spinstates which are opposite one another. For pairs of product functions meeting the above criteria,

$$H_{mn} = -\tfrac{1}{2} J_{jk}, \quad [33]$$

where j and k are the nuclei with opposite spin states. All other off-diagonal terms are zero. Finally, the diagonal elements of $\mathbf{H}$ are given by

$$H_{mm} = -\tfrac{1}{2} \sum_j \delta_j P_{mj} - \tfrac{1}{2} \sum_{j<k} J_{jk} P_{mj} P_{mk}. \quad [34]$$

Once the matrix representations of the $\hat{I}_x$, $\hat{R}_{180x}$, and $\hat{H}$ operators are formed, the calculation of the density matrix (and hence the solution of Eq. [7]) at any n is straightforward. (The calculation of $\exp(-i/2\mathbf{H}\tau)$ and the multiplication and inversion of matrices are simple procedures in MATLAB.) Equation [8] can also be solved by first calculating the transformation matrix that diagonalizes $\exp(-i/2\mathbf{H}\tau)\mathbf{R}\ \exp(-i/2\mathbf{H}\tau)$. We should note however that the transformation matrix generated by MATLAB will not necessarily be orthonormal if $\exp(-i/2\mathbf{H}\tau)\mathbf{R}\ \exp(-i/2\mathbf{H}\tau)$ has degenerate eigenvalues. In such cases, an orthonormal subset of eigenvectors must be created for each degenerate eigenvalue.

ACKNOWLEDGMENT

This work was supported by Grant CA40675 from the NIH.

REFERENCES

1. R. V. Mulkern, S. T. S. Wong, C. Winalski, and F. A. Jolesz, Contrast manipulation and artifact assessment of 2D and 3D RARE sequences, *Magn. Reson. Imaging* **8,** 557–566 (1990).
2. P. S. Melki, R. V. Mulkern, L. P. Panych, and F. A. Jolesz, Comparing the FAISE method with conventional dual-echo sequences, *J. Magn. Reson. Imaging* **1,** 319–326 (1991).
3. R. T. Constable, A. W. Anderson, J. Zhong, and J. C. Gore, Factors influencing contrast in fast spin-echo MR imaging, *Magn. Reson. Imaging* **10,** 497–511 (1992).
4. R. M. Henkelman, P. A. Hardy, J. E. Bishop, C. C. Poon, and D. B. Plewes, Why fat is bright in RARE and fast spin echo imaging, *J. Magn. Reson. Imaging* **2,** 533–540 (1992).
5. J. Listerud and R. V. Mulkern, The *J* coupling hypothesis for bright fat observed on FSE, *in* "Proc., Society of Magnetic Resonance in Medicine 11th annual meeting, New York City," p. 4505 1992.
6. P. S. Melki, F. A. Jolesz, and R. V. Mulkern, Partial RF echo-planar imaging with the FAISE method. II. Contrast equivalence with spin-echo sequences, *Magn. Reson. Med.* **26,** 342–354 (1992).
7. S. Peled, D. S. Williamson, and R. V. Mulkern, Signal intensity studies of strongly-coupled spin systems during CPMG/RARE imaging sequences, *in* "Proc., Society of Magnetic Resonance Third Scientific Meeting, Nice, France," p. 655 1995.
8. D. S. Williamson, R. V. Mulkern, P. D. Jakab, and F. A. Jolesz, Coherence transfer by isotropic mixing in Carr–Purcell–Meiboom–Gill imaging: Implications for the bright fat phenomenon in fast spin-echo imaging, *Magn. Reson. Med.* **35,** 506–513 (1996).
9. R. S. Hinks and D. Martin, Bright fat, fast spin echo, and CPMG, *in* "Proc., Society of Magnetic Resonance in Medicine 11th annual meeting," p. 4503 1992.
10. B. K. Rutt and G. A. Wright, Lipid signal enhancement in CPMG MRI: Effect of field strength, *in* "Proc., Society of Magnetic Resonance in Medicine 11th annual meeting," p. 4504 1992.
11. R. S. Hinks and R. M. Henkelman, Problems with organic materials for magnetic resonance imaging phantoms, *Med. Phys.* **15,** 61–63 (1988).
12. G. A. Wright and A. Macovski, Lipid Signal Enhancement in Spin-Echo Trains, *in* "Proc., Society of Magnetic Resonance in Medicine 11th annual meeting," p. 437 1992.
13. A. Allerhand, Analysis of Carr–Purcell spin echo NMR experiments on multiple-spin systems. I. The effect of homonuclear coupling, *J. Chem. Phys.* **44,** 1–9 (1966).
14. L. E. Kay, J. N. Scarsdale, D. R. Hare, and J. H. Prestegard, Simulation of two-dimensional cross-relaxation spectra in strongly coupled spin systems, *J. Magn. Res.* **68,** 515–525 (1986).
15. P. Güntert, N. Schaefer, G. Otting, and K. Wüthrich, POMA: A complete *Mathematica* implementation of the NMR product-operator formalism, *J. Magn. Res. Ser. A* **3,** 27–45 (1993).
16. B. K. John and R. E. D. McClung, Computer simulations of multiple-pulse and two-dimensional FT NMR experiments, *J. Magn. Res.* **58,** 47–61 (1984).
17. J. Shriver, Product operators and coherence transfer in multiple-pulse NMR experiments, *Concepts Magn. Reson.* **4,** 1–33 (1992).
18. C. P. Slichter, "Principles of Magnetic Resonance," Harper and Row, New York (1963).
19. J. W. Emsley, J. Feeney, and L. H. Sutcliffe, "High Resolution Nuclear Magnetic Resonance Spectroscopy," Pergamon Press, Oxford, UK (1965).
20. A. A. Bothner-By and C. Naar-Colin, The proton magnetic resonance spectra of olefins. I. Propene, butene-1 and hexene-1, *J. Amer. Chem. Soc.* **83,** 231–236 (1961).
21. H. W. Quinn, J. S. McIntyre, and D. J. Peterson, Coordination compounds of olefins with anhydrous silver salts, *Can. J. Chem.* **65,** 2896–2910 (1965).
22. "The Aldrich Library of 13C and 1H FT NMR Spectra," Aldrich Chemical Co., Milwaukee, WI (1993).
23. J. Hennig, A. Nauerth, and H. Friedburg, RARE imaging: A fast imaging method for clinical MR, *Magn. Reson. Med.* **3,** 823–833 (1986).
24. R. T. Constable and J. C. Gore, The loss of small objects in variable TE imaging: Implications for FSE, RARE, and EPI, *Magn. Reson. Med.* **28,** 9–24 (1992).
25. H. Kanazawa, H. Takai, Y. Machida, and M. Hanawa, Contrast naturalization of fast spin echo imaging: A fat reduction technique free from field inhomogeneity, *in* "Proc., SMR, 2nd Meeting, San Francisco," p. 474 1994.
26. L. A. Stables, R. P. Kennan, R. T. Constable, and J. C. Gore, Analysis of *J* coupling induced fat suppression in the DIET sequence, *in* "Proc., ISMRM, 6th Scientific Meeting, Sydney, Australia," p. 1949 1998.
27. R. K. Harris, "Nuclear Magnetic Resonance Spectroscopy: A Physiochemical View," Longman Scientific & Technical, Harlow (1986).